MULTIPLE-POINT GEOSTATISTICS

Stochastic Modeling with Training Images

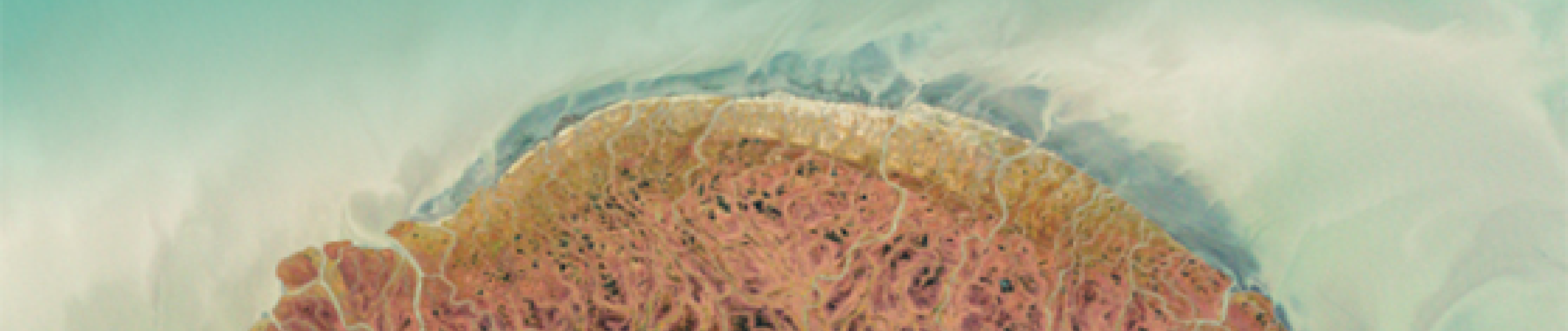

Gregoire Mariethoz • Jef Caers

with website

WILEY Blackwell

Multiple-point geostatistics

Stochastic modeling with training images

Gregoire Mariethoz
Faculty of Geosciences and Environment University of Lausanne, Switzerland

Jef Caers
Energy Resources Engineering Department Stanford University, USA

WILEY Blackwell

This edition first published 2015 © 2015 by John Wiley & Sons, Ltd

Registered office:
John Wiley & Sons, Ltd, The Atrium, Southern Gate, Chichester,
West Sussex, PO19 8SQ, UK

Editorial offices:
9600 Garsington Road, Oxford, OX4 2DQ, UK
The Atrium, Southern Gate, Chichester, West Sussex, PO19 8SQ, UK
111 River Street, Hoboken, NJ 07030-5774, USA

For details of our global editorial offices, for customer services and for information about how to apply for permission to reuse the copyright material in this book please see our website at www.wiley.com/wiley-blackwell

Library of Congress Cataloging-in-Publication Data

Mariethoz, Gregoire, author.
Multiple-point geostatistics : stochastic modeling with training images / Gregoire Mariethoz and Jef Caers.
pages cm
Includes index.

Summary: “The topic of this book concerns an area of geostatistics that has commonly been known as multiple-point geostatistics because it uses more than two-point statistics (correlation), traditionally represented by the variogram, to model spatial phenomena”–Provided by publisher.

ISBN 978-1-118-66275-5 (hardback)
1. Geology–Statistical methods. 2. Geological modeling. I. Caers, Jef, author. II. Title.
QE33.2.S82M37 2015
551.01′5195–dc23

2014035660

A catalogue record for this book is available from the British Library.

Wiley also publishes its books in a variety of electronic formats. Some content that appears in print may not be available in electronic books.

Cover image: Courtesy of NASA Earth Observatory.

CONTENTS

Preface

Acknowledgments

Part I: Concepts

Chapter 1: Hiking in the Sierra Nevada

1.1 An imaginary outdoor adventure company: Buena Sierra

1.2 What lies ahead

Chapter 2: Spatial estimation based on random function theory

2.1 Assumptions of stationarity

2.2 Assumption of stationarity in spatial problems

2.3 The kriging solution

2.4 Estimating covariances

2.5 Semivariogram modeling

2.6 Using a limited neighborhood

2.7 Universal kriging

2.8 Semivariogram modeling for universal kriging

2.9 Simple trend example case

2.10 Nonstationary covariances

2.11 Assessment

References

Chapter 3: Universal kriging with training images

3.1 Choosing for random function theory or not?

3.2 Formulation of universal kriging with training images

3.3 Positive definiteness of the sop matrix

3.4 Simple kriging with training images
3.5 Creating a map of estimates
3.6 Effect of the size of the training image
3.7 Effect of the nature of the training image
3.8 Training images for nonstationary modeling
3.9 Spatial estimation with nonstationary training images
3.10 Summary of methodological differences
References
Chapter 4: Stochastic simulations based on random function theory
4.1 The goal of stochastic simulations
4.2 Stochastic simulation: Gaussian theory
4.3 The sequential Gaussian simulation algorithm
4.4 Properties of multi-Gaussian realizations
4.5 Beyond Gaussian or beyond covariance?
References
Chapter 5: Stochastic simulation without random function theory
5.1 Direct sampling
5.2 The extended normal equation
5.3 Simulation by texture synthesis
References
Chapter 6: Returning to the Sierra Nevada
Reference
Part II: Methods
Chapter 7: Introduction
Chapter 8: The algorithmic building blocks
2.1 Grid and pointset representations

2.2 Multivariate grids
2.3 Neighborhoods
2.4 Storage and restitution of data events
2.5 Computing distances
2.6 Sequential simulation
2.7 Multiple grids
2.8 Conditioning
References
Chapter 9: Multiple-point geostatistics algorithms
3.1 Archetypal MPS algorithm
3.2 Pixel-based algorithms
3.3 Patch-based algorithms
3.4 Qualitative comparison of MPS algorithms
3.5 Postprocessing
References
Chapter 10: Markov random fields
4.1 Markov random field model
4.2 Markov mesh models
4.3 Multigrid formulations
References
Chapter 11: Nonstationary modeling with training images
5.1 Modeling nonstationary domains with stationary training images
5.2 Modeling nonstationary domains with nonstationary training images
References
Chapter 12: Multivariate modeling with training images

6.1 Multivariate and multiple-point relationships
6.2 Multivariate conditional simulation: Implementation issues
6.3 An example
6.4 Multivariate simulation as a filtering problem
References
Chapter 13: Training image construction
7.1 Choosing for training images
7.2 Object-based methods
7.3 Process-based models
7.4 Process-mimicking models
7.5 Elementary training images
7.6 From 2D to 3D
7.7 Training data
7.8 Construction of multivariate training images
7.9 Training image databases
References
Chapter 14: Validation and quality control
8.1 Introduction
8.2 Training image – data validation
8.3 Posterior quality control
References
Chapter 15: Inverse modeling with training images
9.1 Introduction
9.2 Inverse modeling: theory and practice
9.3 Sampling-based methods
9.4 Stochastic search
9.5 Parameterization of MPS realizations

References
Chapter 16: Parallelization
10.1 The need for parallel implementations
10.2 The challenges of parallel computing
10.3 Assessing a parallel implementation
10.4 Parallelization strategies
10.5 Graphical Processing Units
References
Part III: Applications
Chapter 17: Reservoir forecasting – the West Coast of Africa (WCA) reservoir
1.1 Introducing the context around WCA
1.2 Application of MPS to the WCA case
1.3 Alternative modeling workflows
References
Chapter 18: Geological resources modeling in mining
2.1 Context: sustaining the mining value chain
2.2 Stochastic updating of a block model
2.3 An alternative workflow: updating geological contacts
Notes
References
Chapter 19: Climate modeling application – the case of the Murray–Darling Basin
3.1 Introduction
3.2 Presentation of the data set
3.3 Climate model downscaling using multivariate MPS
3.4 Results and validation

References
Index
End User License Agreement

List of Tables

Chapter 1
Table I.1.1
Chapter 3
Table I.3.1
Chapter 4
Table I.4.1
Chapter 8
Table II.8.1
Table II.8.2
Table II.8.3
Chapter 9
Table II.9.1
Chapter 18
Table III.2.1
Table III.2.2
Table III.2.3
Table III.2.4
Table III.2.5
Table III.2.6
Table III.2.7

Table III.2.8

List of Illustrations

Chapter 1

Figure I.1.1 (left) Walker Lake exhaustive digital elevation map (size: 260×300 pixels) grid; and (right) 100 extracted sample data. The colorbar represents elevation in units of ft.

Figure I.1.2 Visualization of the 80 paths taken by hikers of two types: (left) minimal effort; and (right) maximal effort. The color indicates how frequently that portion of the path is taken, with redder color denoting higher frequency.

Figure I.1.3 Histograms of the cumulative elevation gain and path length for the minimal- and maximal-effort hiker. Cumulative elevation gain in units of ft, path length in units of grid cells.

Chapter 2

Figure I.2.1 Example loss functions; the most common choice is the parabola (least squares).

Figure I.2.2 (a) A single unique truth; (b) some sample data taken from it; and (c) its histogram. The goal is to estimate the value at the unsampled location marked with *X*.

Figure I.2.3 (a) Rock density in a homogeneous layer of a carbonate reservoir; and (b) rock density in a heterogeneous deltaic reservoir.

Figure I.2.4 Omnidirectional semivariogram of *Z*.

Figure I.2.5 Semivariogram of the exhaustive Walker Lake data set versus the sample variogram.

Figure I.2.6 (a) Global kriging using all 50 sample data at all estimated locations; (b) a local moving neighborhood; (c) using a minimum of 12 samples; and (d) using penalty. Parts (a–c) are calculated using SGEMS (Remy et al., 2008), and (d) is calculated using the R-package RGeostats.

Figure I.2.7 Simple trend case study: (left) the unknown truth (one realization, see Equation (I.2.38)); and (right) the sample data.

Figure I.2.8 (left) OLS estimate of trend; (middle) a universal kriging estimate based on the OLS estimate of trend; and (right) a universal kriging estimate based on the two-step procedure (using R-package RGeostats).

Chapter 3

Figure I.3.1 An analog data set considered relevant for the domain being modeled. The size of this image (250 × 250) need not be the same as the model grid size.

Figure I.3.2 (a) Artifacts induced by using a moving neighborhood; and (b) corrected by using finite domain kriging and by requiring a minimum of 12 neighboring points.

Figure I.3.3 Comparing the estimates obtained by (a) using a 150 × 150 size training image and (b) using a 250 × 250 size training image.

Figure I.3.4 Minimum error maps (kriging variances) compared to the kriging variance obtained using global ordinary kriging.

Figure I.3.5 (a) Reference case and (b) 100-sample data.

Figure I.3.6 (a–b) Two visually dissimilar training images each with their estimated map from 100 sample data (c–d).

Figure I.3.7 Omnidirectional empirical semivariograms for the two training images (a) Figure I.3.6(a) and (b) Figure I.3.6(b) along with fitted semivariograms using package RGeoS. Both have nugget 0, a range of approximately 35, and sill of 0.985.

Figure I.3.8 (a) An exhaustive DEM deemed representative for the Walker Lake area. The size of the training image is 400 × 400. (b) the result of a simple smoother applied to (a).

Figure I.3.9 (a) A training image for the simple trend case; and (b) its auxiliary variable.

Figure I.3.10 Three nonstationary training images (b) for the simple trend case using the OLS estimate (a) as an auxiliary variable.

Figure I.3.11 Biharmonic spline (a) to create the domain auxiliary variable for the Walker Lake with three nonstationary training images (b–d) generated with direct sampling.

Figure I.3.12 Comparing the estimates obtained by (a) spatial estimation with training images; (b) universal kriging; and (c) ordinary kriging with local moving neighborhood.

Figure I.3.13 The empirical raw (a) and residual (b) semivariograms computed for the nonstationary case. The automatic semivariogram fitting function in RGeostat was used. The number of pairs used for the calculation are plotted next to the experimental semivariogram.

Figure I.3.14 (a) Estimate for Walker Lake using universal kriging with training image in Figure I.3.11(b); (b) path for minimal effort and (c) path for maximal effort.

Chapter 4

Figure I.4.1 (a–c) Three sequential Gaussian simulations of the Walker Lake case.

Figure I.4.2 (a) Exhaustive Walker Lake image; (b) a Gaussian sample constrained to 5% of randomly sampled data from (a); and (c) the same Gaussian law, but now only constrained to 0.1% of the exhaustive image.

Figure I.4.3 (a) Realizations of Walker Lake generated with direct sequential simulation conditioned to 5% of conditioning data; and (b) sequential Gaussian simulation (Figure I.4.2(b)) for comparison. Although DSSIM realizations often show better connected high and low values, they display a similar amorphous character as multi-Gaussian models.

Figure I.4.4 Two Gaussian realizations (G1 and G2) and three rules diagrams (A–C), resulting in unconditional pluri-Gaussian realizations (a–c) (after (Mariethoz et al., 2009).

Chapter 5

Figure I.5.1 (Left) A page from the book *Bouvard et Pécuchet*, by Gustave Flaubert, published in 1881 (English version published by H. S. Nichols in 1896). (Right) a direct sampling realization of one page.

Figure I.5.2 (a–c) Three conditional realizations of Walker Lake digital elevation map using direct sampling.

Figure I.5.3 (a) Walker Lake exhaustive data categorized; (b) corresponding 100 sample data; and (c) training image, categorized.

Figure I.5.4 (a–c) Three SNESIM realizations conditioned to the 100-point data.

Figure I.5.5 Probability maps for each category, (a) lake, (b) foothill and (c) mountain, obtained from calibration on the training image and its auxiliary variable.

Figure I.5.6 (a–c) Three SNESIM realizations constrained to both point data and soft probabilities.

Figure I.5.7 The use of exemplars in computer graphics applications. Models are carved out from unconditional 3D blocks of exemplar-based textures, of size 1024^3 voxels. For computational efficiency, only the voxels that need to be displayed are simulated. 2D exemplars are used to generate 3D models. Exemplars are shown as small inserts (Dong et al., 2008).

Figure I.5.8 Illustration of a basic unconditional "patch-based" algorithm. (a) Training image; (b) set of unique patches extracted from it; (c) stage of simulation where two non-overlapping patches have been simulated; and (d) selection (random) of one of the two patches that best fit (in terms of some distance) the local data event.

Figure I.5.9 Illustration of quilting of two patterns along a raster path.

Figure I.5.10 Illustration of image quilting along a raster path. (a) Raster path starts at some corner; and (b) a next pattern is selected based on a small overlap and quilted with the previous pattern; see Figure I.5.8. (c–d) This procedure is continued along the next row. (e) Training image used for this example.

Figure I.5.11 Three realizations of Walker Lake using image quilting.

Chapter 6

Figure I.6.1 Comparison of the experimental semivariogram of a representative realization from the three sets of realizations considered, along different directions. Blue: east-west semivariograms. Red: north-south semivariograms.

Figure I.6.2 Path statistics (PL = path length, CEG = cumulative elevation gain) calculated for minimal effort for the multi-Gaussian (MG) set.

Figure I.6.3 Path statistics (PL = path length, CEG = cumulative elevation gain) calculated for maximal effort for the multi-Gaussian (MG) set.

Figure I.6.4 Path statistics (PL = path length, CEG = cumulative elevation gain) calculated for minimal effort for the direct-sampling (DS) set.

Figure I.6.5 Path statistics (PL = path length, CEG = cumulative elevation gain) calculated for maximal effort for the direct-sampling (DS) set.

Figure I.6.6 Path statistics (PL = path length, CEG = cumulative elevation gain) calculated for minimal effort for the image-quilting (IQ) set.

Figure I.6.7 Path statistics (PL = path length, CEG = cumulative elevation gain) calculated for maximal effort for the image-quilting (IQ) set.

Figure I.6.8 Elevation along a path taken by a hiker walking on an MG model and a hiker walking on a DS model, for a maximal-effort hiker.

Chapter 8

Figure II.2.1 Regular grid in different dimensions. Top: 1D temporal grid representing 120 years of daily rainfall measures in Sydney, Australia. Middle: 2D grid of a satellite image of the Sundarbans region, Bangladesh. Bottom: 3D grid representing the hydrofacies in an alluvial aquifer in the Maules Creek valley, Australia.

Figure II.2.2 Illustration of the grid representation using IDs. The number inside each cell is the node ID. Blue axis represents the real coordinate system. Red axis represents the coordinate system in units of nodes.

Figure II.2.3 Mask applied over southeastern Australia to limit the modeled area to the landmass and exclude the water bodies.

Figure II.2.4 From left to right: original image, red component, green component, blue component, and the intensity of all three components (corresponding to the norm of a 3D vector), which results in grayscale intensity values.

Figure II.2.5 Representation of colorspaces: (a) RGB colorspace that requires three components; and (b) grayscale space, 1D.

Figure II.2.6 Different types of templates.

Figure II.2.7 A data event corresponding to the rightmost template of Figure II.2.6.

Figure II.2.8 Multivariate template and corresponding multivariate data event.

Figure II.2.9 Illustration of a convolution for a binary variable.

Figure II.2.10 Illustration of a convolution for a continuous variable. From left to right: original image, pattern sought for, convolution result, and threshold-based selection. The two right images are the result of a convolution of the left image using the pattern *N*. *N* is enlarged 30 times for better visualization. On the convolution figure, dark values represent lower convolution values (hence, high similarity with *N*).

Figure II.2.11 Tree-based classification of the different life forms. From Haeckel, E. (1866). *Generelle Morphologie der Organismen: allgemeine Grundzüge der organischen Formen-Wissenschaft, mechanisch begründet durch die von C. Darwin reformirte Decendenz-Theorie*, Berlin, downloaded from http://en.wikipedia.org/wiki/Ernst_Haeckel

Figure II.2.12 Schematic representation of tree storage for a binary variable and a simple four-node template.

Figure II.2.13 Example TI and all of the individual data events that compose it, considering a simple four-node template.

Figure II.2.14 Complete search tree with all counters corresponding to the storage of the TI shown in Figure II.2.13.

Figure II.2.15 Search tree omitting zero-occurrence counters, corresponding to the storage of the TI shown in Figure II.2.13.

Figure II.2.16 Compact search tree with collapsing of singleton branches, corresponding to the storage of the TI shown in Figure II.2.13.

Figure II.2.17 Data events storage in a list, corresponding to the storage of the TI shown in

Figure II.2.13.

Figure II.2.18 Representation of the filters used in the FILTERSIM algorithm and illustration of the computation of a filter score for a given data pattern. Modified from Zhang, T., et al. (2006). With kind permission from Springer Science and Business Media.

Figure II.2.19 Representation of a pattern database in a distance space. The patterns originating from the TI (left) are represented in 2D space (right). Figure (a) from Honarkhah and Caers (2010). With kind permission from Springer Science and Business Media.

Figure II.2.20 A TI and two realizations (from a total of 50) generated with three algorithms: DISPAT, CCSIM (see Chapter II.3), and sequential indicator simulations (SISIMs; Deutsch and Journel, 1992).

Figure II.2.21 Cluster-histograms of patterns (CHPs) derived by first clustering the patterns of the TI, then classifying the patterns of the realizations based on these clusters. Each image is a prototype representing a cluster of patterns, and the numbers above each prototype are the frequencies associated to this cluster for each of the four cases considered (TI, DISPAT, CCSIM, and SISIM).

Figure II.2.22 Spatial cumulants of orders 3, 4, and 5 computed on a simple binary image. Next to each cumulant map, the corresponding lag vectors are displayed. Reprinted from Mustapha, H. and R. Dimitrakopoulos (2010). With permission from Elsevier.

Figure II.2.23 Illustration of the Hausdorff distance between two sets A and B.

Figure II.2.24 Examples of geometric transformations applied to *N*. (a) Original data event *N*. (b) 45° rotation. (c) 80° rotation. (d) Factor 2 affinity along the *X*-axis. (e) Factor 0.5 affinity along the *X*-axis. Modified from Huysmans, M. and A. Dassargues (2011). With kind permission from Springer Science and Business Media.

Figure II.2.25 Illustration of the use of proximity transform as a more relevant comparison between patterns. (a) Patterns compared by counting the number of mismatching nodes. (b) The same patterns after proximity transform can be compared using an Euclidean norm, which is more appropriate to distinguish the distance between the objects compared.

Figure II.2.26 Separation in indicators to compute proximity transforms on patterns having more than two categories. (a) Multicategory pattern, (b) transformation into indicators, and (c) proximity transform on indicators (modified from Arpat, 2005).

Figure II.2.27 (a) Fine-scale shale layers, (b) connected components, (c) derived coarse grid with edges, (d) indicator of presence of bottom edge, (e) indicator of presence of right edge, (f) combined edges code, (g) coding of edges. Modified from Huysmans and Dassargues (2011).

Figure II.2.28 Steps of a sequential simulation with a random path.

Figure II.2.29 Illustration of the random simulation path.

Figure II.2.30 Left: typical L-shaped template used for unilateral simulation starting in the lower-left corner. Right: conditioning with a unilateral path. The causal part of the template is in white, and the noncausal part is in pink. Informed nodes (conditioning data) are shown in green.

Figure II.2.31 Illustration of the unilateral simulation path with the direction $+X+Y$.

Figure II.2.32 The effect of the path on the simulation. Training image (Ganges delta, Bangladesh), and simulation with random and two unilateral paths in different directions. Simulations obtained with the direct sampling algorithm.

Figure II.2.33 Illustration of a patch-based simulation with a unilateral path.

Figure II.2.34 Principle of multiple grids. The left column shows a simulation grid with the nodes belonging to each multigrid level in a different color. The right column shows the five-node templates corresponding to each level (template for the first level is not shown).

Figure II.2.35 Illustration of the effect of using or not using multiple grids, with the same TI as in Figure II.2.32. Simulations obtained with the SNESIM algorithm.

Figure II.2.36 Servosystem with different intensities applied to a 1D Brownian motion.

Chapter 10

Figure II.4.1 (a) Representation of a graph; (b) a graph representation of a 3×3 neighborhood in the grid; and (c) the various clique configurations of a 3×3 neighborhood.

Figure II.4.2 (a) Asymmetric neighborhood definition and model formulation in MMM; and (b) an example of choices on a neighborhood where higher-order interaction is considered: the arrows indicate the direction and the order in which interaction increases (after Stien & Kolbjørnsen, 2011).

Figure II.4.3 Application of an MMM model to a simple 2D binary training image. Results courtesy of Odd Kolbjørnsen.

Figure II.4.4 Single-grid (left) versus multigrid (right) ordering of the cells for the MMM formulation. In the coarsest grid of the multigrid ordering, nodes 1 to 9 are colored green. Note that the same neighborhood configuration can be maintained, rendering parameter estimations more practical (modified from Kolbjørnsen et al., 2014).

Figure II.4.5 Training image and simulated MMM models. Results courtesy of Odd Kolbjørnsen (see also Kolbjørnsen et al., 2014).

Chapter 11

Figure II.5.1 Three cases illustrating nonstationarity in 1D: (a) stationary, (b) nonstationary with varying mean, and (c) nonstationary with variable variance.

Figure II.5.2 Example of 2D nonstationarity based on a satellite image of the Sundarbans region, Bangladesh. (a) high-order nonstationarity in continuous values, where both the univariate distribution and the type of patterns vary from the bottom to the top of the domain. (b) Similar type of nonstationarity for a categorical variable.

Figure II.5.3 Nonstationary modeling using zones with separate TIs. (a) The two TIs used. (b) The prescribed zone for each TI. (c) One resulting nonstationary realization.

Figure II.5.4 Nonstationary modeling using zones using a continuous transition in the probability of using a TI. (a) Two TIs used. (b) Probability of choosing TI1 (black) or TI2 (white). (c) One resulting nonstationary realization. (d) A posteriori map indicating which TI was used for the simulation of each node.

Figure II.5.5 The use of rotation and affinity zones with SNESIM. Reprinted from Liu, Y. (2006). With permission from Elsevier.

Figure II.5.6 Nonstationarity modeling with probability aggregation using a soft probability map. A uniform rotation of 45° is applied to the TI patterns, and a tau = 1 is used with SNESIM. Reprinted from Liu, Y. (2006). With permission from Elsevier.

Figure II.5.7 Simulation using a mean-invariant distance. (a) Multi-Gaussian stationary TI. (b) Nonstationary data set (100 points data), with values in a different range than those of the TI. (c) One simulation with a mean-invariant distance. Circles represent the location of the 100 conditioning data (Mariethoz et al., 2010).

Figure II.5.8 A nonstationary simulation is obtained based on a stationary elementary TI and a rotation tolerance field. The arrows in the channels allow visualizing the rotation of the TI patterns.

Figure II.5.9 Rotation-invariant distances applied to a 3D case (Mariethoz and Kelly, 2011). (a) Rotation field, interpolated based on discrete values (angles shown in degrees). (b and c) Two possible elementary TIs (categorical and continuous). (d and e) Two corresponding realizations.

Figure II.5.10 Illustration of using a nonstationary TI (a) without explicit nonstationary modeling. The nonstationary patterns are evenly used on the entire simulation domain, resulting in a stationary simulation (b) with degraded spatial features.

Figure II.5.11 Nonstationarity modeling using control maps. Given a, a' and b', the simulation algorithm generates b, which is a nonstationarity simulation presenting the same patterns as in a, and the same relationship with b' than the relation a : a'.

Figure II.5.12 Nonstationarity modeling using control maps (a′ b′), with a different nonstationarity in the simulation (b) and in the TI (a).

Chapter 12

Figure II.6.1 Illustration of a multivariate convolution involving different types of variables. Variable 1: red band; variable 2: green band; variable 3: blue band; and variable 4: delineation of two categories of color intensity values (high intensity in black and low intensity in white).

Figure II.6.2 Trivariate reference case. (a) Variable 1: a transformed multi-Gaussian field (Zinn and Harvey, 2003). (b) Variable 2: moving average and shifting applied to variable 1. (c) Variable 3: smoothing, then thresholding of variable 1.

Figure II.6.3 (a–c) Scatterplots of all co-located values, with variables considered two by two. Lower half of the figure: conditional histograms illustrating the co-located relationship with binary variable 3.

Figure II.6.4 3D scatterplot of all three variables in the reference.

Figure II.6.5 The data available and the scatterplots based on 50 collocated sample locations. Lower part of the figure: conditional histograms to better illustrate the relationship with binary variable 3.

Figure II.6.6 (a–c) Multivariate training images.

Figure II.6.7 (a–c) Scatterplot of all co-located values in the training image, with variables considered two by two. Lower half of the figure: conditional histograms to better illustrate the relationship with binary variable 3.

Figure II.6.8 3D scatterplot of all three variables in the training image.

Figure II.6.9 (a–c) Reference (identical to Figure II.6.2), shown here for comparison. (d–f) One multivariate conditional realization obtained using direct sampling. (g–i) The average of 10 conditional realizations.

Figure II.6.10 (a–c) Scatterplot of all co-located values in one realization. Lower half of the figure: conditional histograms to better illustrate the relationship with binary variable 3.

Figure II.6.11 3D scatterplot of all three variables in the realization.

Figure II.6.12 Illustration of the image analogy notation with a by-example filtering application. Modified from Hertzmann, A., C. E. Jacobs, et al. (2001).

Figure II.6.13 Identification of geological structures from a georadar survey. A and A′: training image (Bayer et al., 2011). B′: another georadar survey taken in a similar geological environment. B:

simulated photograph honoring the relationship B : B′.

Figure II.6.14 Scatterplots of (a) the multivariate training images and (b) multivariate realization of Figure II.6.13.

Chapter 13

Figure II.7.1 A simple object-based model of channelized structures. Image obtained with the TiGenerator software (Maharaja, 2008). Grid size: 250×250×100 nodes.

Figure II.7.2 An object-based model considering variable channel width and depth, randomized sinuosity, and different facies for the various architectural elements (main channel and levees). Image obtained with the FLUVSIM software (Deutsch and Tran, 2002). Grid size: 250×250×100 nodes.

Figure II.7.3 Process-based reconstruction of the Alameda Creek alluvial fan. Reprinted from Paleoclimatic signature in terrestrial flood deposits. Science 256(5065): 1775–1782. With permission from AAAS.

Figure II.7.4 (a) Process-based modeling from tank experiments (data courtesy of Saint Anthony Falls Laboratory, University of Minnesota). (b) Interpretation from the overhead photos (data courtesy of Siyao Xu).

Figure II.7.5 A process-mimicking model of an alluvial reservoir using the FLUMY simulation method (Lopez et al., 2008). The spatial organization of the structural elements is based on physical equations. Grid size: 500×500×200 nodes.

Figure II.7.6 Process-based (data courtesy of Exxon) versus process-mimicking models (Michael et al., 2010).

Figure II.7.7 Left: elementary training image (size: 50×50×50 nodes). Right: one realization using rotation-invariant distances (size: 180×150×120 nodes). Rotation-invariant distances are considering angles of +/− 90° in all directions.

Figure II.7.8 Left: elementary training image (size: 50×50×50 nodes). Right: one realization using rotation-invariant distances (size: 180×150×120 nodes). Rotation-invariant distances are considering angles of +/− 20° in all directions.

Figure II.7.9 Merging of compatible orthogonal data events. Modified/Reprinted from Comunian, A., P. Renard, et al. (2012). With permission from Elsevier.

Figure II.7.10 Method of perpendicular sections. (a) Orthogonal training images. (b) The first sections simulated are those that intersect at the location of conditioning data (wells). (c) The remaining sections are generated sequentially until (d) the entire 3D volume is simulated (modified from Kessler et al., 2013).

Figure II.7.11 Reconstruction of a partial image based on the principle of training data. (a) Infrared satellite data of the Pacific Ocean presenting gaps (source: National Oceanic and Atmospheric Administration (NOAA)). (b) One reconstruction simulation based on (a); here, the data are used as both training data and conditioning data. Dark blue represents gaps, and darker blue represents continents.

Figure II.7.12 (a) Lithological facies. (b) Sediment grain size. (c) Sediment age since the time of deposition.

Figure II.7.13 A multivariate training image made of (a) a hydraulic conductivity field; and (b–f) snapshots of contaminant distribution at different time stamps.

Chapter 14

Figure II.8.1 Illustration case involving as data: one well, three possible training images, and two possible trend models.

Figure II.8.2 (a) Single synthetic well datum; (b) another synthetic well datum; (c) smoothing of the first well datum; (d) smoothing of the second well datum; (e) MDS plot based on the Euclidean distance between the smoothed data; and (f) MDS plot based on the Jensen–Shannon distance of the MPHs for each well datum. Black crosses are the field well data.

Figure II.8.3 Illustration of the concept of connected components based on the Tropical Rainfall Measuring Mission (TRMM) data, shown in (a). The continuous variable representing accumulated rainfall in (b) is converted to the binary variable (c) on which a connected component analysis is applied (d); 1793 connected components are found for the category corresponding to rainfall >1 mm/12 hours.

Figure II.8.4 Illustration of the connectivity function based on the connected component analysis of Figure II.8.3.

Figure II.8.5 Illustration of coherence maps for three test cases. All cases are unconditional DS realizations, with fraction of training image, $f = 1$, threshold $t = 0$. (a) A categorical variable with $n = 40$

neighbor nodes. (b) A continuous variable with n = 20 neighbor nodes. (c) The same continuous variable with n = 60 neighbor nodes. The color codes in the coherence maps represent the IDs of the nodes in the training image.

Figure II.8.6 Illustration of multiscale pyramids of a single model.

Figure II.8.7 Case with a two wells (a) and simple binary 3D stationary training image (b). Realization of both CCSIM (c) and SNESIM (d) from a set of 50 realizations with each method.

Figure II.8.8 Top: local ANODI. Bottom: MDS plot from global ANODI.

Figure II.8.9 Ensemble average for 50 CCSIM realizations; and 50 SNESIM realizations.

Chapter 15

Figure II.9.1 A Gaussian prior and a simple tracer problem. A tracer is injected at the left location, and its arrival monitored at the right location. Various Gaussian models are sampled from which the tracer response is calculated.

Figure II.9.2 Studying the convergence of the gradual deformation when changing the concentration curves to earlier and later breakthrough times.

Figure II.9.3 An example of a new MPS realization generated with SNESIM (c), based on an existing one (a), using a spatial resampling of data points as well as constrained to existing conditioning data at four well locations (b). (d) Training image. The realization grid is of dimension 100×100×40, and the training image of dimension 150×200×80.